Chapter 5
Heat and Mass Transfer in Rotating Cone-and-Disk Systems for Laminar Flows

5.1 General Characterization of the Problem

In the past, non-rotating conical diffusers (Fig. 5.1) were modeled using simplified Navier–Stokes equations without flow pre-swirl at the inlet [1]. Flow pre-swirl effects on the heat transfer were for the first time studied by the author of this work [2].

Cone-and-plate devices, where flow develops in a gap with small angles $\gamma = 1\ldots0.5°$ between a rotating cone and a stationary plate (Fig. 5.2), are used in viscosimetry [3–5]. Medicine employs such devices for nurturing endothelial cells that grow as a monolayer on the non-rotating plate, whereas a cone rotates slowly to renew the feeding fluid and simultaneously not to damage the cells [6–8].

Flow regimes in cone-and-plate devices were studied experimentally [8], simulated using CFD codes [3, 8] and using perturbation techniques [5–7]. Self-similar Navier–Stokes and energy equations were derived and solved by the author of this work [2, 9–11].

Convective heat transfer in cone-and-disk configurations, with one of them rotating or both co-rotating/contra-rotating, along with a stationary conical diffuser, depends strongly on the radial temperature distribution on the disk [2, 9, 10]. Simulations were done mostly for air ($Pr = 0.71$); new phenomena in heat and mass transfer for other values of the Prandtl and Schmidt numbers were first investigated by the author in [11].

For the small angle γ, the Navier–Stokes Eqs. (2.1)–(2.3) can be simplified [5–7] for the considered laminar flow

$$-\frac{v_\varphi^2}{r} = -\frac{1}{\rho}\frac{\partial p}{\partial r} + \nu\frac{\partial^2 v_r}{\partial z^2}, \tag{5.1}$$

$$v_r\frac{\partial v_\varphi}{\partial r} + v_z\frac{\partial v_\varphi}{\partial z} + \frac{v_r v_\varphi}{r} = \nu\frac{\partial^2 v_\varphi}{\partial z^2}, \tag{5.2}$$

I.V. Shevchuk, *Modelling of Convective Heat and Mass Transfer in Rotating Flows*, Mathematical Engineering, DOI 10.1007/978-3-319-20961-6_5

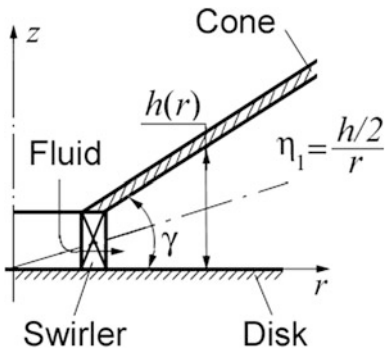

Fig. 5.1 Schematic of swirling flow in a stationary conical diffuser [9]

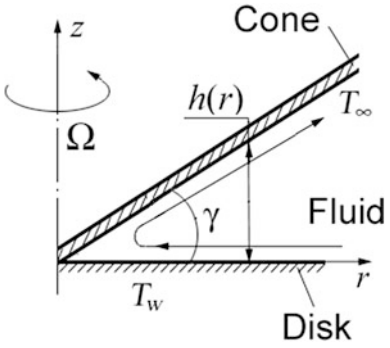

Fig. 5.2 Schematic of fluid flow in a gap with a rotating cone and a stationary disk [9]

$$-\frac{1}{\rho}\frac{\partial p}{\partial z}+\nu\frac{\partial^2 v_z}{\partial z^2}=0. \tag{5.3}$$

A perturbation solution of Eqs. (5.1)–(5.3) by the method of expansion in the small parameter $Re = Re_\Omega \eta_1^2/12$ (where $\eta_1 = h/r$) yields [5]

$$v_r/(\Omega r) = Re(1.8\tilde{z}^2 - \tilde{z}^4 - 0.8\tilde{z}), \tag{5.4}$$

$$v_\varphi/(\Omega r) = \tilde{z} + Re^2(-83\tilde{z} + 70\tilde{z}^4 + 63\tilde{z}^5 - 50\tilde{z}^7)/175, \tag{5.5}$$

$$v_z/(\Omega r) = Re\eta_1(\tilde{z}^2 - \tilde{z}^3). \tag{5.6}$$

Based on Eqs. (5.4) and (5.5), one can derive expressions for the flow swirl angle on the surface of a stationary disk φ_w, whereas a cone is rotating

$$\varphi_w = \arctan[0.8Re/(1 - 83Re^2/175)] \quad \text{for } Re = 0 - 1.452, \tag{5.7}$$

$$\varphi_w = \arctan(0.8Re) \quad \text{for } Re \ll 1. \tag{5.8}$$

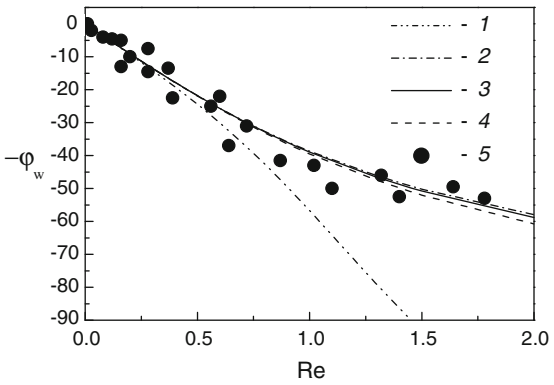

Fig. 5.3 Flow swirl angle on the surface of a stationary disk with a rotating cone [9]. Computations: *1*—Eq. (5.7); *2*—Eq. (5.8) [5]; *3*—self-similar Eqs. (5.19)–(5.22) [10]; *4*—self-similar Eqs. (5.24)–(5.26) [10]. Data *5*—experiments [5]

Equation (5.7) agrees well with measurements [5] and Eq. (5.8) just for $Re \leq 0.5$ (Fig. 5.3). Equation (5.8) that formally holds just for $Re \ll 1$ correlates nevertheless with the measurements up to $Re = 2$. Authors [5] deduced only Eq. (5.8), whereas Eq. (5.7) automatically stemming from Eqs. (5.4) and (5.5) was ignored in [5]. At $Re = 1.452$, Eq. (5.7) predicts the value $\varphi_w = 90°$, whereas the expression in brackets of the function arctan tends effectively to infinity; this contradicts to the physics of the problem.

A series expansion in the small parameter Re, with up to 70 terms, were used also in the works [6, 7] to solve Eqs. (5.1)–(5.3). However, the parameter φ_w predicted by the authors [6, 7] deviated from experiments [5] at $Re = 0.5$–1 more noticeably than Eq. (5.8). In addition, the parameter φ_w predicted in [6, 7] at $Re = 1.2928$ exhibits an asymptotical trend to infinity contradictive to the physics of the problem.

This chapter summarizes results of simulations of convective heat transfer in the geometries "stationary conical diffuser" (Fig. 5.1) and "rotating cone-and-disk" without initial flow swirl (Fig. 5.2). Such pioneering studies based on full self-similar forms of the Navier–Stokes equations together with the thermal boundary layer equation have been for the first time performed by the author of the present work [2, 9–11].

5.2 Self-similar Navier–Stokes and Energy Equations

Considering a steady-state axisymmetric laminar flow and heat transfer, we will solve the Navier–Stokes Eqs. (2.1)–(2.3) and the reduced Eqs. (5.1)–(5.3) together with the energy Eq. (2.12) for laminar flow. For the configurations "rotating cone-and-disk" without initial swirl, the boundary conditions are given by

$$z = 0: \quad v_r = 0, \quad v_z = 0, \quad v_\varphi = \omega r, \quad T_w - T_\infty = c_0 r^{n_*}, \tag{5.9}$$

$$z = h: \quad v_r = 0, \quad v_z = 0, \quad v_\varphi = \Omega r, \quad T = T_\infty. \tag{5.10}$$

For the geometry "stationary conical diffuser," the boundary conditions are given by

$$z = 0: \quad v_r = v_\varphi = v_z = 0, \quad T_w - T_\infty = c_0 r^{n_*}, \tag{5.11}$$

$$z = z_1 = h/2: \quad v_r = v_{r1}, \quad v_\varphi = v_{\varphi 1}, \quad \mathrm{d}v_r/\mathrm{d}z = 0, \quad T = T_\infty. \tag{5.12}$$

Here, c_0 and n_* are the constants, while the conditions at $z = z_1 = h/2$ are denoted with a subscript "1." We will study convective heat transfer of a *disk* (but not a cone) under the wall boundary conditions (5.9) and (5.11) that match with Eq. (2.30) for a single disk.

The exponent n_* in Eqs. (5.9) and (5.11) takes negative, zero, or positive values $-2 \le n_* \le 4$. Cone heat/mass transfer is unimportant for the current study; therefore, the temperature T_∞ and the concentration C_∞ on the surface of the cone are assumed to be constant and equal to those of the fluid at infinity. In case of convective diffusion in bioengineering applications, the boundary concentration on the plate/disk C_w is lower than that on the cone/infinity C_∞, because endothelial cells digest feeding culture from the fluid.

The boundary layer equation for the temperature is used instead of the full energy equation; this model assumption is justified above in Chaps. 2–4.

Self-similar variables and functions enable simplifying partial differential Eqs. (2.1)–(2.3), (5.1)–(5.3) and (2.12) and translating them to ordinary non-linear differential equations to be solved numerically with the help of the software like Mathcad [1, 12–17].

Self-similar variables and functions can be derived with the help of group theory [2, 9, 10]. Let us enter a linear transformation of differential equations

$$\begin{aligned} r &= A^{\alpha_1}\overline{r}, \quad z = A^{\alpha_2}\overline{z}, \quad v_r = A^{\alpha_3}\overline{v}_r, \\ v_\varphi &= A^{\alpha_4}\overline{v}_\varphi, \quad v_z = A^{\alpha_5}\overline{v}_z, \quad p = A^{\alpha_6}\overline{p}, \end{aligned} \tag{5.13}$$

with α_k (k = 1, …, 6) and the parameter of transformation A being constants [12]. Transformations (5.13) are substituted into Eqs. (2.1)–(2.3), (5.1)–(5.3) and (2.12). If the exponents at the constant A are identical for every summand, this means that the non-transformed and transformed equations are invariant, which yields

$$\alpha_1 = \alpha_2 = \alpha, \quad \alpha_3 = \alpha_4 = \alpha_5 = -\alpha, \quad \alpha_6 = -2\alpha, \tag{5.14}$$

$$\begin{aligned} A &= \left(\frac{r}{\overline{r}}\right)^{1/\alpha} = \left(\frac{z}{\overline{z}}\right)^{1/\alpha} = \left(\frac{\overline{v}_r}{v_r}\right)^{1/\alpha} \\ &= \left(\frac{\overline{v}_\varphi}{v_\varphi}\right)^{1/\alpha} = \left(\frac{\overline{v}_z}{v_z}\right)^{1/\alpha} = \left(\frac{\overline{p}}{p}\right)^{1/(2\alpha)}, \end{aligned} \tag{5.15}$$

$$\overline{z}/z = \overline{r}/r, \quad \overline{v}_r\overline{r} = v_r r, \quad \overline{v}_\varphi\overline{r} = v_\varphi r, \quad \overline{v}_z\overline{r} = v_z r, \quad \overline{p}\cdot\overline{r}^2 = p\cdot r^2. \tag{5.16}$$

Morgan's theorem states [12] that Eq. (5.16) serve as similarity variables, if the boundary conditions are independent of the coordinate r.

The self-similar variables and functions were formulated using Eqs. (5.15) and (5.16)

$$\eta = z/r, \quad F = v_r r/v, \quad G = v_\varphi r/v, \quad H = v_z r/v, \tag{5.17}$$

$$P = pr^2/(\rho v^2), \theta = (T - T_\infty)/(T_w - T_\infty). \tag{5.18}$$

Function θ does not change its form because of the linearity of the energy equation. Substituting Eqs. (5.17) and (5.18) into Eqs. (2.1)–(2.3) and (2.12), one can deduce

$$F^2 + G^2 + 2P + F'L + \eta P' + F''M = 0, \tag{5.19}$$

$$G'L + G''M = 0, \tag{5.20}$$

$$P' - H(1 + F) - H'L - H''M = 0, \tag{5.21}$$

$$H' - \eta F'' = 0, \tag{5.22}$$

$$\theta'' = \mathrm{Pr}[n_* F\theta + \theta'(H - \eta F)]. \tag{5.23}$$

Here, $M = 1 + \eta^2$ and $L = 3\eta + \eta F - H$. In ordinary differential Eqs. (5.19)–(5.23), primes denote derivatives with respect to the η-coordinate.

A substitution of Eqs. (5.17) and (5.18) into Eqs. (5.1)–(5.3) gives

$$G^2 + 2P + \eta P' + F'' = 0, \tag{5.24}$$

$$G'(\eta F - H) + G'' = 0, \tag{5.25}$$

$$P' = H''. \tag{5.26}$$

Boundary conditions (5.9) and (5.10) can be rewritten as

$$\eta = 0: \quad F = H = 0, \quad G = G_0, \quad \theta = 1, \tag{5.27}$$

$$\eta = \eta_1: \quad F = H = 0, \quad G = G_1, \quad \theta = 0, \tag{5.28}$$

with $\eta_1 = h/r$, $G_0 = Re_\omega = \omega r^2/v$, $G_1 = Re_\Omega = \Omega r^2/v$.

Boundary conditions (5.11) and (5.12) can be rearranged as

$$\eta = 0: \quad F = G = H = 0, \quad \theta = 1, \tag{5.29}$$

$$\eta = \eta_1: \quad G = G_1, \quad F = F_1, \quad F' = 0, \quad \theta = 0. \tag{5.30}$$

Here, $\eta_1 = 0.5h/r$, and subscripts "0" and "1" denote functions at $\eta = 0$ and $\eta = \eta_1$, accordingly.

Boundary conditions (5.27) and (5.28) for the functions $G_0 = Re_\omega$ and $G_1 = Re_\Omega$ are r-dependent and do not comply with the self-similarity requirements that the self-similar functions must be constant at the boundaries. Self-similar fuctions are Eq. (5.29) ($G_0 = 0$) for a stationary disk and Eq. (5.30) with $G_1 = \text{const.}$, $F_1 = \text{const.}$, which imply the free vortex laws for the velocity components v_r and v_φ in the middle of the stationary conical diffuser

$$(v_\varphi)_{\eta=\eta_1} = G_1 v/r, \quad (v_r)_{\eta=\eta_1} = F_1 v/r. \tag{5.31}$$

We treat here Eqs. (5.27) and (5.28) as locally self-similar, with G_0 and G_1 being parameters at each specific r-coordinate [2, 10]. As demonstrated beneath, this model yields the results that are in good agreement with experiments and theoretical predictions.

5.3 Rotating Disk and/or Cone

5.3.1 Numerical Values of Parameters in the Computations

The Mathcad software has been used to obtain a numerical solution of Eqs. (5.19)–(5.26). Angles of conicity for the simulations were $\gamma = 4°$ (small $\eta_1 = 0.0698$) and $\gamma = 45°$ (relatively large $\eta_1 = 1$). The value of η_1 varying over the span of $\gamma = 1$–$5°$ was shown to have no influence on the results of simulations.

Values of the Prandtl and Schmidt numbers were $Pr = Sc = 0.1$–100 for a configuration with a rotating cone and a stationary disk, $Pr = Sc = 0.1$–800 for a stationary cone and a rotating disk, and $Pr = Sc = 0.71$ for the rest of the geometries. In the simulations, the value of $Re = Re_\omega \eta_1^2/12$ (or $Re = Re_\Omega \eta_1^2/12$) was set to be unity, which yields $Re_\Omega = 12$, $Re_\omega = 12$ at $\eta_1 = 1$, and $Re_\omega = 2463$, $Re_\Omega = 2463$ at $\eta_1 = 0.0698$. The exponent n_* in Eq. (5.23) took negative, zero, or positive values $-2 \le n_* \le 4$ that enable modeling different radially decreasing, constant, or increasing distributions of T_w on the disk surface.

5.3.2 Rotating Cone and Stationary Disk

Figures 5.4, 5.5, and 5.6 depict velocity profiles predicted in [9] for $Re = 1$ ($Re_\omega = 2463$) by Eqs. (5.19)–(5.22), (5.24)–(5.26) and those computed in the work [5] with a help of the method of expansion in the small parameter Re.

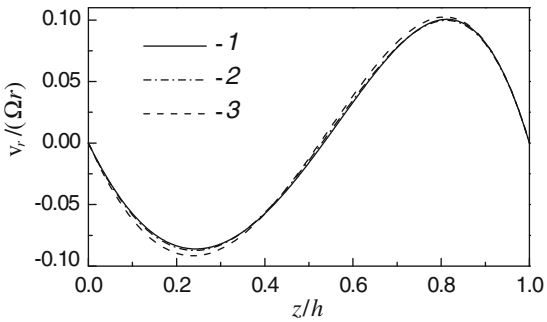

Fig. 5.4 Profiles of the radial velocity component in a gap between a rotating cone and a stationary disk [9]. *1*—Eqs. (5.19)–(5.22); *2*—Eqs. (5.24)–(5.26); *3*—Eq. (5.4) [5]

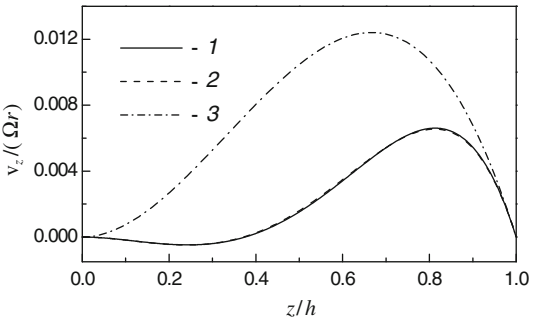

Fig. 5.5 Profiles of the axial velocity component in a gap between a rotating cone and a stationary disk [9]. *1*—Eqs. (5.19)–(5.22); *2*—Eqs. (5.24)–(5.26); *3*—Eq. (5.6) [5]

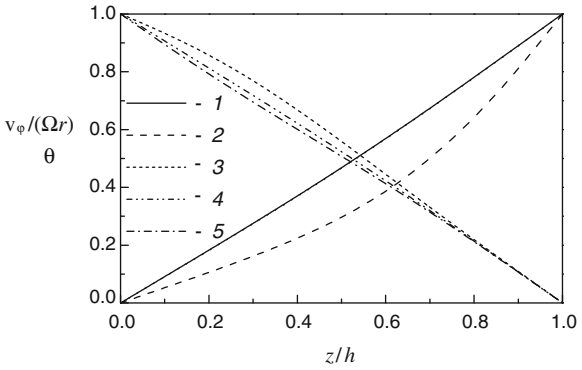

Fig. 5.6 Profiles of the tangential velocity component (*1, 2*) and temperature θ (*3–5*) in a gap between a rotating cone and a stationary disk [9]. *1*—Eqs. (5.19)–(5.22) and (5.24)–(5.26); *2*—Eq. (5.5) [5]; *3*—Eqs. (5.19)–(5.23) at $n_* = 2$; *4*—(5.19)–(5.23) at $n_* = 0$; *5*—(5.19)–(5.23) at $n_* = -1$

The axial velocity component (Fig. 5.5) is an order of magnitude smaller than the radial velocity component (Fig. 5.4), which, in turn, is an order of magnitude smaller than the tangential velocity component (Fig. 5.6). Curves predicted by Eqs. (5.19)–(5.22) and (5.24)–(5.26) practically merge, which certifies validity of the simplified Eqs. (5.24)–(5.26) for small angles of conicity γ. Data of [5] for the radial velocity v_r agree well with the simulations in Fig. 5.4; however, discrepancies between the data of [5] and the simulations for components v_z and v_φ are more distinct (Figs. 5.5 and 5.6).

To validate the accuracy of the simulations of the tangential velocity, experimental data [5] and predictions [9] for the flow swirl angle on the disk surface $\varphi_w = \arctan[v_r/(\Omega r - v_\varphi)]_{z=0} = \arctan(-F'_w/G'_w)$ were compared. Predictions and experiments correlate for the Reynolds number depicted in Fig. 5.3. It can be also concluded that the velocity profiles in Figs. 5.4, 5.5, and 5.6 predicted by Eqs. (5.19)–(5.22) and (5.24)–(5.28) model the flow in the gap more realistically than those by Eqs. (5.4)–(5.8) [5].

Figure 5.6 shows temperature profiles in the gap computed at for $Pr = 0.71$. The temperature curves demonstrate the decreasing trend from unity at the disk surface to zero at the cone wall. The form of the curves is affected by the value of n_*. Near the disk, derivatives of the θ profiles diminish with increasing n_*.

To compute the local Nusselt number, the following expression was used:

$$Nu = \frac{q_w r}{\lambda(T_w - T_\infty)} = -\theta'_{\eta=0}. \tag{5.32}$$

To enable comparisons with Eqs. (3.4) and (3.5) for the rotating disks, the Nusselt number may be rearranged using a derivative with respect to the variable $\zeta = z\sqrt{\Omega/\nu}$

$$Nu = K_1 Re_\Omega^{1/2} \tag{5.33}$$

$$K_1 = \frac{-(\mathrm{d}\theta/\mathrm{d}\eta)_{\eta=0}}{Re_\Omega^{1/2}} = -\left(\frac{\mathrm{d}\theta}{\mathrm{d}\zeta}\right)_{\zeta=0}. \tag{5.34}$$

Based on these expressions, it was calculated at $\eta_1 = 0.0698$ (or $Re_\Omega = 2463$) that $Nu = 15.28$, 13.40, 9.35 and $K_1 = 0.308$, 0.270, 0.188 at $n_* = -1$, 0, 2, accordingly. These values of the coefficient K_1 match fairly well with those for a single rotating disk (see Table 3.8). For larger values of n_*, the coefficient K_1 diminishes, which is observed in centripetal flow over a stationary disk imposed by a rotating cone (to compare, an increase in the coefficient K_1 together with n_* occurs in centrifugal flow over a rotating disk, see Chaps. 3 and 4).

Given $\eta_1 = 1$ and $Re = 1$ (or $Re_\Omega = 12$), the Nusselt numbers are $Nu = 1.047$, 0.954, 0.760 with $K_1 = 0.302$, 0.275, 0.219 for the same exponents n_*. One can conclude that the coefficient K_1 is conservative and only weakly dependent on the conicity angle γ.

5.3.3 Rotating Disk and Stationary Cone

Radial flow pattern here is opposite to that considered above: the flow is centripetal over the cone, and centrifugal over the disk (Fig. 5.7).

The tangential velocity v_φ demonstrates a trend linearly subsiding from a disk toward a cone, while the profile of axial velocity component v_z looks mirror-symmetrical as compared to the v_z profile in Fig. 5.5. The temperature profile θ in Fig. 5.7 for $Pr = 0.71$ almost merges with the $v_\varphi/(\omega r)$ curve.

To compute the Nusselt number at the disk, Eqs. (5.32)–(5.34) are again employed; as $\Omega = 0$, it must be replaced with ω while defining the Re number and coordinate ζ. Based on this, the calculated Nusselt numbers for $\eta_1 = 0.0698$, $Re = 1$ ($Re_\omega = 2463$) are $Nu = 13.33, 15.35, 19.13$ and $K_1 = 0.269, 0.309, 0.386$ at $Pr = 0.71$, and $n_* = -1, 0, 2$, accordingly. It is evident that the coefficient K_1 is an increasing function of n_*. However, the rate of increase is lower than that for a single rotating disk, where $K_1 = 0.189, 0.326, 0.519$ for the identical values n_* (Table 3.1). Given $\eta_1 = 1$ and $Re = 1$ ($Re_\omega = 12$), the computed Nusselt numbers are $Nu = 0.96, 1.041, 1.197$ and $K_1 = 0.277, 0.301, 0.345$ for identical exponents n_* and $Pr = 0.71$. Thus, the coefficient K_1 is again very weakly dependent on the conicity angle γ.

5.3.4 Effects of Prandtl and Schmidt Numbers

Effects of the Prandtl or Schmidt numbers are considered for the geometries with a rotating disk and stationary cone or a stationary disk and a rotating cone [11].

Rotating disk and stationary cone. As the Pr numbers increase, curves of the temperature profiles θ for $n_* = 0$ and $n_* = -1$ shift downward exhibiting a non-linear

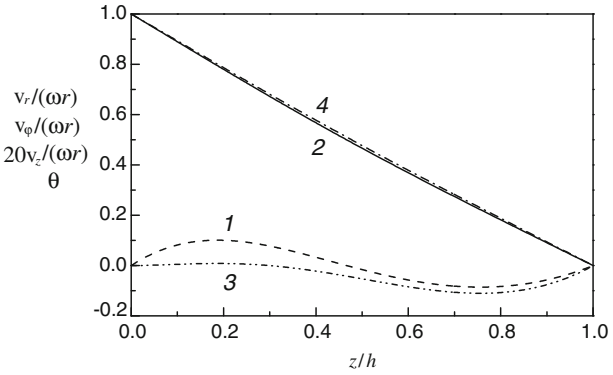

Fig. 5.7 Velocity and temperature profiles in the gap between a rotating disk and a stationary cone at $Re = 1$ ($Re_\omega = 2463$) and $\eta_1 = 0.0698$ [9]. *1*—$v_r/(\omega r)$; *2*—$v_\varphi/(\omega r)$; *3*—$20v_z/(\omega r)$; *4*—$\theta(Pr = 0.71, n_* = 0)$

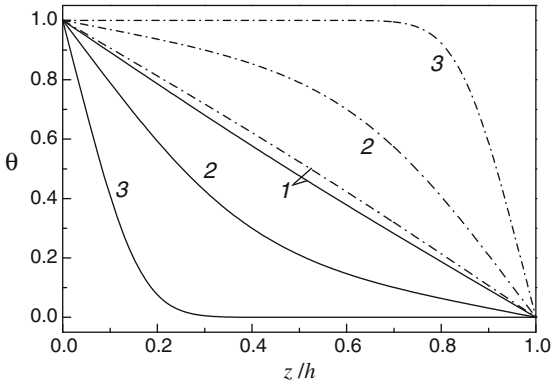

Fig. 5.8 Temperature profiles θ in the gap for $n_* = 0$ [11]. *Solid lines* rotating disk and stationary cone. *Dash-dot lines* stationary disk and rotating cone. *1*—$Pr = 0.71$; *2*—$Pr = 10$; *3*—$Pr = 100$

trend of variation due to diminished heat conduction, whereas the function θ at $Pr \geq 100$ becomes zero inside the gap between the cone and the disk (Figs. 5.8 and 5.9). For $n_* \geq 0$, curves of θ demonstrate qualitatively analogous trend. With respect to the profiles of θ for $n_* = -1$, the condition $d\theta/d\eta \rightarrow 0$ in the vicinity of the cone is attained already at $Pr \geq 20$ (Fig. 5.9).

Over the range $0 \leq n_* \leq 4$, the constant K_1 increases with the Prandtl number (Table 5.1); the trend persists also at $n_* = -0.5$, i.e., when negative gradient dT_w/dr is weak.

As seen from Table 5.1, signs of v_r and dT_w/dr become different and coefficient K_1 diminishes for larger Prandtl numbers, when the wall temperature gradient dT_w/dr is strongly negative ($n_* = -1$). Let us write the coefficient K_1 at $n_* = 0$ as follows:

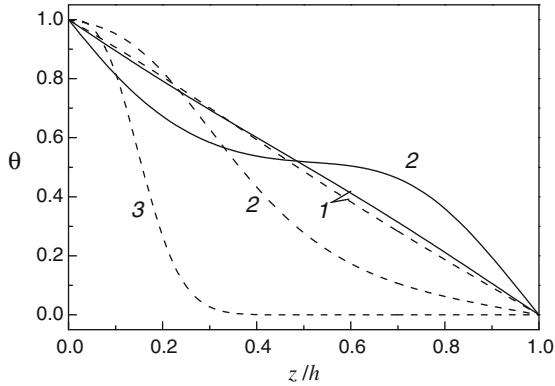

Fig. 5.9 Temperature profiles θ in the gap for $n_* = -1$ [11]. *Dashed lines* rotating disk and stationary cone. *Solid lines* stationary disk and rotating cone. *1*—$Pr = 0.71$; *2*—$Pr = 10$; *3*—$Pr = 100$

Table 5.1 Coefficient K_1, for rotating disk and stationary cone [11]

$Pr(Sc)$	$n_* = -1$	$n_* = -0.5$	$n_* = 0$	$n_* = 1$	$n_* = 2$	$n_* = 4$
0.1	0.2858	0.2887	0.2915	0.2972	0.3029	0.3141
0.5	0.2745	0.2890	0.3032	0.3309	0.3579	0.4094
0.71	0.2687	0.2892	0.3094	0.3483	0.3855	0.4556
1.0	0.2607	0.2898	0.3180	0.3718	0.4225	0.5155
5.0	0.1650	0.3155	0.4447	0.6552	0.8172	0.9048
10.0	0.0842	0.3829	0.6082	0.9265	0.9860	1.5737
50	0.00008	0.8744	1.3572	1.9492	2.3432	2.8986
100	0.0	1.1745	1.7882	2.5295	3.0225	3.7184
400	0.0	2.0005	2.9876	4.1627	4.9419	6.0423
800	0.0	2.5742	3.8435	5.3051	6.2862	7.6717

$$K_1 = K_{1,Pr=1} Pr^{m_p}, \tag{5.35}$$

where $K_{1,Pr=1} = 0.318$. This enables determining a function for the exponent $m_p(Pr)$ presented in Table 5.2, whose asymptotic limit is $m_p = 0.372$ for high Prandtl numbers. To compare, this limit for a single rotating disk is $m_p = 1/3$ at $Pr \to \infty$ [9] (see Chap. 6).

Rotating cone and stationary disk. Profiles of θ for $n_* = 0$ and $n_* = -1$ at $Pr = 0.71$ span practically linear between unity on the disk surface and zero on the cone wall; further, for larger Prandtl numbers, profiles of θ shift upward demonstrating a non-linear trend of variation owing to reduced heat conduction (Figs. 5.8 and 5.9). For $Pr \geq 100$, the derivative $d\theta/d\eta$ in the vicinity of the disk exhibits zero values.

For $n_* > 0$, $Pr \leq 1$ and $n_* = -1$, $Pr \leq 1$, curves of θ practically merge with the profile predicted for $Pr = 0.71$, $n_* = 0$. Curves of θ demonstrate a S-shape at $n_* = -1$ and $Pr = 1$–10 (Fig. 5.9). Profiles of θ become non-physical at $Pr > 1$, $n_* > 0$ and $Pr > 10$, $n_* = -1$.

For larger Pr numbers and $n_* < 0$, the constant K_1 increases (because signs of v_r and dT_w/dr are the same); at $n_* \geq 0$, the coefficient K_1 diminishes due to the opposite signs of v_r and dT_w/dr (Table 5.3).

Application to the cone-and-plate devices. The results described in Sect. 5.3.4 become applicable to mass transfer upon replacement of T, Pr, Nu with C, Sc, Sh,

Table 5.2 Exponent m_p in Eq. (5.35) at T_w = const., rotating disk, and stationary cone [11]

$Pr(Sc)$	0.71	0.9	1.1	2	2.28	2.4	2.5	10
m_p	0.0805	0.0901	0.0978	0.1319	0.1409	0.1446	0.1476	0.2817
$Pr(Sc)$	100	200	400	600	800			
m_p	0.375	0.3752	0.3739	0.3729	0.3724			

Table 5.3 Coefficient K_1, rotating cone, and stationary disk [11]

$Pr(Sc)$	$n_* = -1$	$n_* = -0.5$	$n_* = 0$	$n_* = 1$	$n_* = 2$	$n_* = 4$
0.1	0.2913	0.2887	0.2860	0.2807	0.2752	0.2643
0.5	0.3021	0.2889	0.2755	0.2479	0.2193	0.1587
0.71	0.3078	0.2892	0.2700	0.2302	0.1883	0.0971
0.9	0.3130	0.2894	0.2651	0.2140	0.1593	0.0373
1.0	0.3158	0.2896	0.2625	0.2054	0.1436	0.0040
2.0	0.3436	0.2924	0.2375			
10.0	0.5712	0.3679	0.0895			
50			0.0001			
100			0.0			

respectively. Here, data for K_1 at $n_* = 0$ from Tables 5.1, 5.2, and 5.3 are to be used, since the wall boundary condition for mass transfer is $C_w = \text{const}$. [9]. It is evident that the coefficients K_1 for a stationary disk and a rotating cone are always smaller than the K_1 values for a rotating disk and a stationary cone. This difference becomes more pronounced at larger Schmidt numbers and is equal to 14.6 % at $Sc = 0.71$; 2.6 times at $Sc = 5$; 46.1 times at $Sc = 20$, and asymptotically tends to infinity in the limit at infinite Schmidt numbers.

Thus, one can enhance efficiency of a cone-and-plate device used in bioengineering for nurturing endothelial cells spread on the plate via assigning the disk to rotate and fixing the cone instead of the currently used devices "rotating cone—stationary plate."

5.3.5 *Co-rotating Disk and Cone*

Here, the ratio between the Re_Ω and Re_ω numbers makes a crucial influence on the flow pattern. If $Re_\Omega > Re_\omega$ (cone revolves faster), fluid flow over the cone is centrifugal, and centripetal over the disk. If $Re_\Omega < Re_\omega$ (disk revolves faster), a reverse flow pattern emerges. Equations (5.32)–(5.34) (reference angular speed Ω) were used to compute the Nusselt number for $Pr = 0.71$. A situation with approximately the same angular speeds of a disk and a cone was considered. Given $Re_\omega = 1.01 Re_\Omega$, Eqs. (5.32)–(5.34) yield $Nu = 14.31$, 14.35, 14.43 and $K_1 = 0.288$, 0.289, 0.291; given $Re_\omega = 0.99 Re_\omega$, one can obtain $Nu = 14.35$, 14.31, 14.23 and $K_1 = 0.289$, 0.288, 0.287 at $n_* = -1$, 0, 2, accordingly. In both cases, we pre-set $Re = 1$ and $\eta_1 = 0.0698$ ($Re_\Omega = 2463$). The computed Nusselt numbers were $Nu = 0.999$, 1.001, 1.004 and $K_1 = 0.288$, 0.289, 0.290 at $Re_\omega = 1.01 Re_\Omega$, $Re = 1$ and $\eta_1 = 1$ ($Re_\Omega = 12$).

The coefficient K_1 is practically the same for all considered cases. For larger values of n_*, Nusselt numbers increase in centrifugal flow over the disk and decrease in centripetal flow. Variation of the conical spacing practically does not affect the coefficient K_1.

5.3.6 *Counter-Rotating Disk and Cone*

The most complex flow pattern emerges here with centrifugal flow over a disk and a cone and centripetal flow in the center of the conical cavity (Fig. 5.10). The axial velocity v_z is negative in the vicinity of the walls and positive in the center of the gap; the tangential velocity $v_\varphi/(\Omega r)$ behaves as a linear function increasing between -1 and 1, whereas the temperature function θ at $Pr = 0.71$ monotonically diminishes from unity to zero.

Given $\eta_1 = 0.0698$, $Re = 1$, and $Re_\omega = -Re_\Omega = 2463$, profile of v_r is symmetrical relative to the center of the gap (curve 2, Fig. 5.10).

Equations (5.32)–(5.34) (reference velocity Ω) were used to compute the Nusselt number for $Pr = 0.71$. Nusselt number increases with n_* over the disk surface: $Nu = 14.21$, 14.44, 14.85 and $K_1 = 0.286$, 0.201, 0.299 at $n_* = -1$, 0, 2. The conditions $\eta_1 = 1$, $Re = 1$, $Re_\omega = 12$, and $Re_\Omega = -12$ yield a non-symmetrical radial velocity profile v_r, since the radial flow is stronger near the cone (curve 4, Fig. 5.8). As a result, increasing n_* is accompanied with a decreasing Nusselt number on the disk: $Nu = 1.011$, 0.989, 0.942 and $K_1 = 0.292$, 0.285, 0.272, given the same set of the n_* values as that used above.

Thus, here heat transfer is almost insensitive to the value and sign of dT_w/dr on the disk surface. Variation of the conical gap spacing and revolution speeds of a cone and a disk influence on the v_r profile and qualitative trend of the dependence of Nu on n_*.

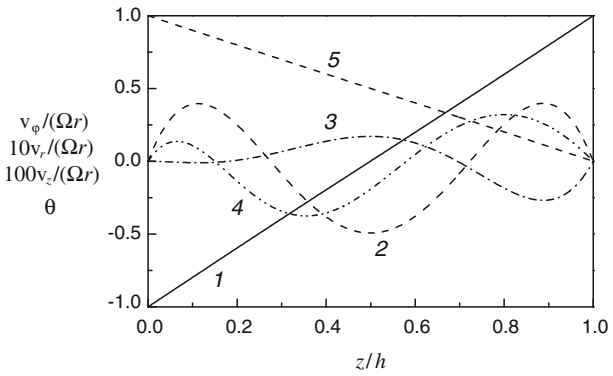

Fig. 5.10 Counter-rotating disk and a cone at $Re = 1$ [9]: *1*—$v_\varphi/(\omega r)$; *2*, *4*—$10v_r/(\omega r)$; *3*—$100v_z/(\omega r)$; *5*—θ ($Pr = 0.71$, $n_* = 0$). Here *1–3*—$Re_\omega = -Re_\Omega = 2463$ and $\eta_1 = 0.0698$; *4*—$Re_\omega = -Re_\Omega = 12$ and $\eta_1 = 1$

5.4 Radially Outward Swirling Flow in a Stationary Conical Diffuser

A non-rotating diffuser with conicity of $\gamma = 35°$ or $\eta_1 = 0.35$ was studied here (Fig. 5.2). The physical interpretation of Eqs. (5.30) and (5.31) is that they describe a free vortex expanding along the centerline of the gap. In practice, potential flow in the form of a free vortex spans over a significant height of the conical gap pushing the boundary layers toward the walls. Hence, Eqs. (5.30) and (5.31) describe a somewhat idealized vortex flow pattern.

Simulations demonstrated that non-swirling purely radial flow ($G_1 = 0$) does not undergo separation from the walls at $F_1 < 63$. Separation starts at $F_1 \approx 63$, whereas at $F_1 > 63$, a pronounced recirculation flow region is visible over the disk (Fig. 5.11).

Responsible for the onset of separation is the large conicity of the diffuser: a reduced conicity $\eta_1 = 0.035$ shifts the separation value of F_1 to about 7500. Flow swirl ($G_1 = 97.96$, $Re = G_1\eta_1^2/12 = 1$) causes accentuated recirculation region over the disk (Fig. 5.11).

Given a zero radial velocity $F_1 = 0$ at the inlet to the diffuser, the radial velocity v_r becomes negative over the entire gap height excluding the point $\eta = \eta_1$ (curve 6 in Fig. 5.11; $|F|_{\max}$ relates to the minimum point of the plot of $F/|F|_{\max}$ at $\eta/\eta_1 \approx 0.4$, i.e., $F_{\max} = -24.28$). For larger values of F_1, the recirculation area reduces, whereas the centrifugal flow area near the center of the conical gap grows up. The tangential velocity G/G_1 shows a linear distribution between 0 at $\eta = 0$ (disk) and 1 (cone) for $\eta = \eta_1$ (curve 1 in Fig. 5.12).

The diffuser is used to restore the static pressure, which grows with r as the velocity components $(v_r)_{\eta=\eta_1}$ and $(v_\varphi)_{\eta=\eta_1}$ decrease. To ensure self-similarity of the function P in Eq. (5.18), the quantity P must denote the excess pressure $p–p_\infty$,

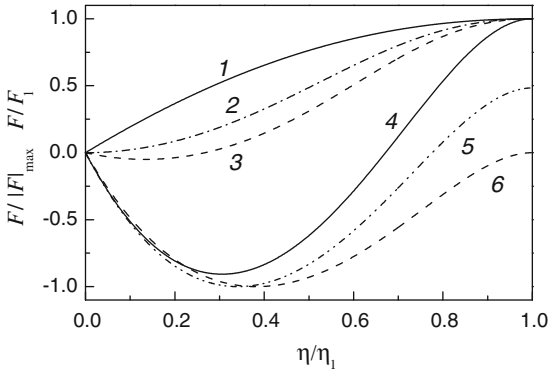

Fig. 5.11 Profiles of the radial velocity F/F_1 (*1–4*) or $F/|F|_{\max}$ (*5*, *6*) in a gap between a disk and a cone [9]. $\boldsymbol{G_1 = 0}$: *1*—$F_1 = 2$; *2*—$F_1 = 63$; *3*—$F_1 = 90$. $\boldsymbol{G_1 = 97.96}$: *4*—$F_1 = 20$; *5*—$F_1 = 10$, $|F|_{\max} = 20.66$; *6*—$F_1 = 0$, $|F|_{\max} = 24.28$

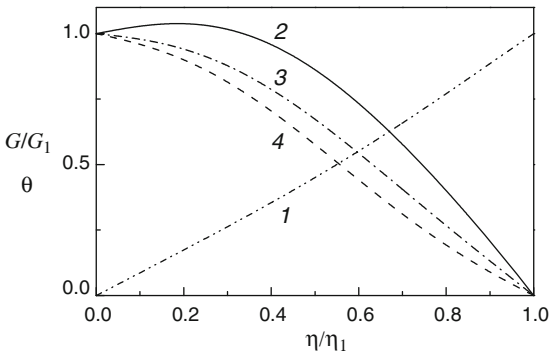

Fig. 5.12 Profiles of the tangential velocity component G/G_1 and temperature θ in the gap between a cone and a disk [9]. *1*—G/G_1 for $F_1 = 30$, $G_1 = 97.96$; *2*—θ for $G_1 = 97.96$ and $F_1 = 10$; *3*—θ for $G_1 = 97.96$ and $F_1 = 30$; *4*—θ for $G_1 = 97.96$ and $F_1 = 60$ ($Pr = 0.71$, $n_* = 2$)

where $p = p_\infty = \text{const.}$ for $r \to r_\infty$. Thus, the parameter P shows the pressure recovery level; in non-swirling flow ($G_1 = 0$), P increases with F_1 (Fig. 5.13).

Flow swirl $G_1 = 97.96$ entails noticeable additional augmentation of the pressure recovery parameter P, whereas the contribution of F_1 in the range $F_1 = 0$–20 is rather insignificant. As can be seen from Fig. 5.14, curves $Nu(F_1)$ computed by Eq. (5.32) for $F_1 = 50$–63 demonstrate maxima at $n_* = 2$ and 0 and minima at $n_* = -1$.

For non-swirling flow ($G_1 = 0$) and non-zero inlet radial velocity F_1, the Nusselt numbers increase together with the exponent n_* (curves 1–3, Fig. 5.14).

If the exponent n_* remains within the range $n_* = 0$–2 and the radial velocity F_1 increases, the Nusselt numbers (a) demonstrate a trend of augmentation under the conditions of non-separating centrifugal flow, (b) stay practically constant, if the function F_1 approaches the onset of separation, and (c) show a reduction for centripetal secondary flow over the disk (curves 1 and 2 in Fig. 5.14). These trends become rather insignificant at $n_* = 0$.

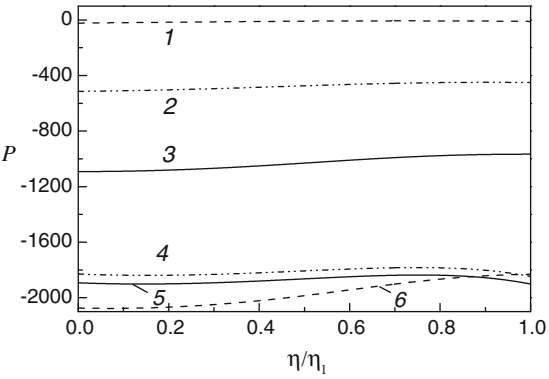

Fig. 5.13 Static pressure drop in the gap for $G_1 = 0$ (curves *1*–*4*) and $G_1 = 97.96$ (curves *5*, *6*) [9]. *1*, *6*—$F_1 = 20$; *2*—$F_1 = 45$; *3*—$F_1 = 63$; *4*—$F_1 = 90$; *5*—$F_1 = 10$

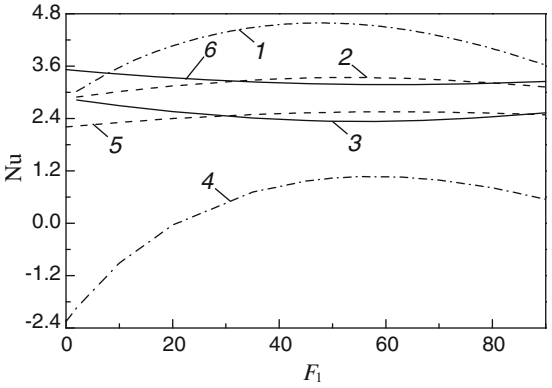

Fig. 5.14 Nusselt numbers in the gap for $G_1 = 0$ (curves *1–3*) and $G_1 = 97.96$ (curves *4–6*) [9]. *1*, *4*—$n_* = 2$; *2*, *5*—$n_* = 0$; *3*, *6*—$n_* = -1$

Flow with initial swirl $G_1 = 97.96$ demonstrates different signs of v_r and dT_w/dr accompanied with reduced Nusselt numbers at $n_* = 2$ and 0 (curves 4 and 5 in Fig. 5.14) as compared to the flow without swirl. Given $n_* = -1$, signs of v_r and dT_w/dr become the same, accompanied with increased Nusselt numbers (curve 6 in Fig. 5.14) as compared to non-swirling fluid. Although, for $G_1 = 97.96$ and increasing F_1, the radially inward flow persists in the vicinity of the disk, the shapes of the curves 4, 5, and 6 for $Nu(F_1)$ are analogous to curves 1, 2, and 3 plotted for non-swirling flow for the same values of n_* (see Fig. 5.14).

Temperature profiles 2 and 3 in Fig. 5.12 for swirling flow ($G_1 = 97.96$) and $n_* = 2$ show a decreasing behavior at $F_1 > 21$. For $F_1 \leq 21$, the temperature curve 4 in Fig. 5.11 exhibits a maximum near the wall, if fluid flows centripetally in the direction of the decrease in T_w. This causes the Nusselt number curve 4 in Fig. 5.14 to become negative: the disk is heated by the fluid (whereas positive Nu numbers mean fluid heated by a disk).

To conclude, in this chapter, self-similar solutions of the Navier–Stokes and energy equations were derived for fluid flow in a conical gap depicted in Figs. 5.1 and 5.2. Simulations were performed for the cases "rotating cone–stationary disk," "rotating disk–stationary cone," "co-rotating or contra-rotating disk and cone," and "non-rotating conical diffuser." Effects of the boundary conditions and various Prandtl/Schmidt numbers on the pressure, velocity, and temperature pattern, as well as on the Nusselt/Sherwood numbers, were studied.

References

1. Schlichting G (1968) Boundary-layer theory. McGraw-Hill Book Company, New York
2. Shevchuk IV (2004) Laminar heat transfer of a swirled flow in a conical diffuser. Self-similar solution. Fluid Dyn 39(1):42–46
3. Fewell ME, Hellums JD (1977) The secondary flow of Newtonian fluids in cone and plate viscometers with small gap angles. Trans Soc Rheol 21(4):535–565
4. Mooney M, Ewart RH (1934) The conicylindrical viscometer. Physics 5:350–354

5. Sdougos HP, Bussolari SR, Dewey CF (1984) Secondary flow and turbulence in a cone-and-plate device. J Fluid Mech 138:379–404
6. Buschmann MH (2002) A solution for the flow between a cone and a plate at low Reynolds number. J Thermal Sci 11(4):289–295
7. Buschmann MH, Dieterich P, Adams NA, Schnittler H-J (2005) Analysis of flow in a cone-and-plate apparatus with respect to spatial and temporal effects on endothelial cells. Biotechnol Bioeng 89(5):493–502
8. Sucosky P, Padala M, Elhammali A, Balachandran K, Jo H, Yoganathan AP (2008) Design of an ex vivo culture system to investigate the effects of shear stress on cardiovascular tissue. Trans ASME J Biomech Eng 130(3): Paper 035001
9. Shevchuk IV (2009) Convective heat and mass transfer in rotating disk systems. Springer, Berlin
10. Shevchuk IV (2004) A self-similar solution of Navier–Stokes and energy equations for rotating flows between a cone and a disk. High Temp 42(1):95–100
11. Shevchuk IV (2011) Laminar heat and mass transfer in rotating cone-and-plate devices. Trans ASME J Heat Transf 133(2): Paper 024502
12. Cebeci T, Bradshaw P (1984) Physical and computational aspects of convective heat transfer. Springer, Berlin
13. Dorfman LA (1963) Hydrodynamic resistance and the heat loss of rotating solids. Oliver and Boyd, Edinburgh
14. Owen JM, Rogers RH (1989) Flow and heat transfer in rotating-disc systems. In: Rotor-stator systems, vol 1. Research Studies Press Ltd., Taunton
15. Shevchuk IV (1998) Simulation of heat transfer in a rotating disk: the effect of approximation of the tangent of the angle of flow swirling. High Temp 36(3):522–524
16. Shevchuk IV (2001) Effect of the wall temperature on laminar heat transfer in a rotating disk: an approximate analytical solution. High Temp 39(4):637–640
17. Shevchuk IV (2002) Laminar heat transfer in a rotating disk under conditions of forced air impingement cooling: approximate analytical solution. High Temp 40(5):684–692